Acta Polytechnica CTU Proceedings **55**:71–79, 2025
https://doi.org/10.14311/APP.2025.55.0071

Published by the Czech Technical University in Prague

DISPERSION TYPE METAL-METAL BASED HIGH-DENSITY FUELS FOR NUCLEAR REACTORS – SAMPLE PREPARATION, ANALYSIS AND EXAMINATION OF LOCA BEHAVIOUR

Petr Šárek[a,b,*], Jakub Krejčí[b], Tomáš Chmela[b], Jitka Kabátová[b]

[a] *Czech Technical University in Prague, Faculty of Mechanical Engineering, Department of Material Engineering, Karlovo náměstí 13, 121 35 Prague 2 – Nové Město, Czech Republic*

[b] *UJP PRAHA a.s., Nad Kamínkou 1345, 156 00 Prague 16 – Zbraslav*

[*] corresponding author: sarek@ujp.cz

Abstract. Metal-based nulear fuels have been proposed as an alternative to UO_2 partly in response to increasing pressure to continually improve nuclear system safety. In this work, a set of High-Density Fuel samples manufactured from depleted uranium alloys and Zr-based matrix have been manufactured and evaluated in the as-manufactured and post-LOCA conditions. A qualitative analysis of the samples showed that the matrix and fuel behaviour is mostly consistent with theory and available research while quantitative analysis revealed a major impact of fuel element geometry on packing density and distribution. Fuel–matrix–cladding interactions of varying intensity have also been observed during fabrication and under LOCA conditions.

Keywords: Accident Tolerant Fuel, High-Density Fuel, nuclear fuel, dispersion fuel, metallic uranium.

1. Introduction

Accident Tolerant Fuels (ATF) can generally be divided into concepts that improve safety by modifying either the cladding or the fuel itself (see Figure 1). High-Density Fuels (HDF) substitute more traditional sintered UO_2 ceramic pellets with materials (either compounds or metal alloys) that offer higher fissile material density and significantly improved thermal conductivity. While an increase in fissile material content enables a better neutron economy and higher burn-up at comparable encrichment levels, improved thermal conductivity helps to reduce the temperature gradient across the fuel rod during operation, enhances performance during transient conditions and reduces the release of gaseous fission products.

While non-metallic HDFs, such as sintered UC or UN, allow for a "drop-in" replacement of current systems, their safety profile is questionable due to a high level of reactivity with water. Upon direct contact with water, uranium carbide reacts pyrophorically according to Equation 1 forming uranium dioxide and methane gas or other light hydrocarbons [1].

$$UC + 2H_2O \rightarrow UO_2 + CH_4. \quad (1)$$

Uranium nitride behaves similarly forming U_3O_8, ammonia and hydrogen gas as seen in Equation 2 [2].

$$6UN + 16H_2O \rightarrow 2U_3O_8 + 6NH_3 + 7H_2. \quad (2)$$

Metal-based HDFs require a distinct design philosophy. While sintered ceramics can be used as monolithic pellets, metal alloys generally exhibit more pronounced radiation swelling and fission gas accumulation, which can lead to cracking and fuel-cladding interactions even at relatively low burnup levels. These challenges

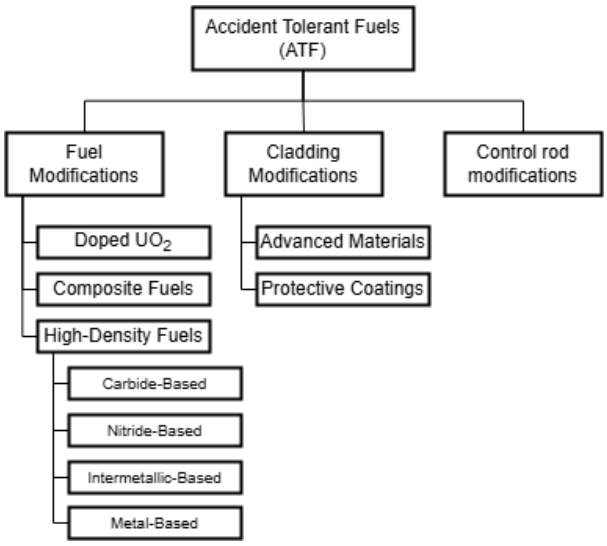

Figure 1. Classification of ATF concepts based on fuel system modification strategies.

gave rise to the concept of dispersion fuels, where discrete fuel particles/segments are embedded in a non-fissile porous matrix rather than formed into homogenous pellets as illustrated in Figure 2 to accomodate swelling and gas release [3].

2. Materials and methods

2.1. Fuel alloy selection and element preparation

Several depleted uranium-based alloys were selected based on their potential to meet the performance requirements of advanced nuclear fuels. Pure uranium offers the maximum achievable uranium density, but

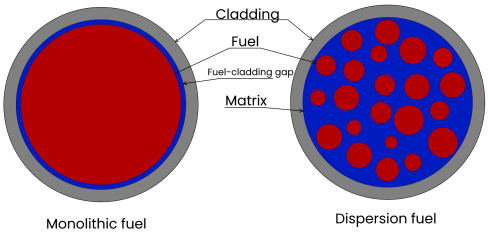

Figure 2. Illustration of monolithic (left) and dispersion (right) fuel.

Material	Geometry	Equivalent diameter
Uranium	Cylindrical	∼2.5 mm
U-9Mo	Cubic	<2.5 mm
U-4Si	Irregular	∼2 mm
Tungsten	Spherical	2 mm

Table 1. Selected fuel materials and element geometry.

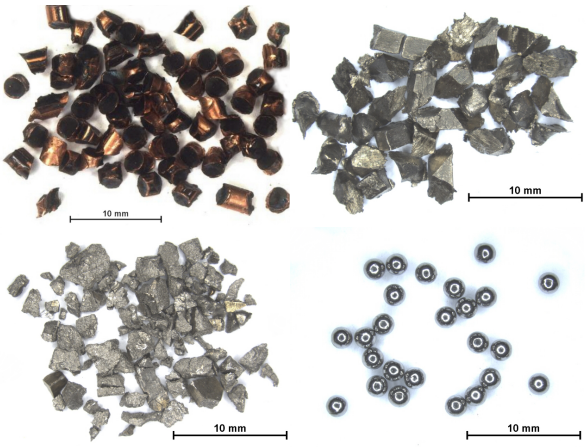

Figure 3. Uranium (top left), U-Mo (top right), U-Si (bottom left) and W (bottom right) elements.

its poor dimensional stability and high swelling tendency limit its practical application. U-Mo alloys, particularly those containing 7–10 wt % Mo, exhibit reduced radiation swelling, fission gas accumulation, and enhanced mechanical stability under irradiation due to γ phase stabilisation. U-Si alloys, on the other hand, combine a high volumetric fraction of intermetallic compounds within a solid-solution uranium matrix [3].

The selected materials, along with the corresponding element geometry and dimensions, are listed in Table 1. Pure uranium was available as a 2.5 mm diameter copper-coated wire, which was sheared into 1.5–2 mm long elements. The U-Mo alloy was milled into 2×2 mm square cross section wire and sheared into 1–2 mm long elements. U-Si is notably hard and brittle which complicates machining operations. As such, larger sections of U-Si bulk were cut from castings, cooled to −196 °C using liquid nitrogen, and subsequently shattered into small fragments of irregular size and shape. The crushed material was then sieved to obtain a 1–3 mm fraction.

While not a fissile material, 2 mm diameter spheres manufactured from a high-density Tungsten pseudoalloy were sourced to simulate ideal fuel element geometry. An overview of the manufactured fuel element simulators can be seen in Figure 3.

2.2. Matrix alloy and cladding

2.2.1. Matrix alloy synthesis

The Zr–8Fe–8Cu tertiary eutectic was selected as the matrix alloy due to its favorable combination of thermal, metallurgical, and neutronic properties. Its low melting point of around 850 °C enables consistent low-temperature fabrication while maintaining sufficient thermal margin for reactor operation (see Figure 4). The alloy exhibits good metallurgical compatibility with both U-based fuels and common Zr-based cladding materials, reducing the risk of deleterious interfacial reactions. Compared to alternative Zr–Fe-Be systems, the inclusion of Cu in place of Be comes with reduced cost, lack of associated Beryllium toxicity and improved handling safety while still providing acceptable, albeit worse, neutronic and mechanical performance [4].

Pure metals (>99.9 % purity) were weighed according to the target composition and melted using an arc furnace under an inert, low pressure helium atmosphere. The resulting casting was re-melted until satisfactory homogenity was achieved yielding an ingot for further processing. This ingot, shown in Figure 5, was subsequently machined into cylindrical rods with an external diameter of less than 9 mm, suitable for use in a supersonic gas atomization process to produce the final alloy powder, which was sieved to a <100 µg fraction for analysis and sample fabrication. Documentation of the resulting powder along with chemical analysis can be found in Section 3.2.

2.2.2. Cladding selection

Two types of Zr-1Nb alloy cladding (denoted A and B) of differing dimensions were sectioned into segments with one side recieving a welded endcap. Cladding A (B) has a nominal inner and outer diameter of 7.95 mm (10.9 mm) and 9.10 mm (12.9 mm) respectively. Based on these values, the internal volume of each cladding segment for volumetric ratio calculations can be approximated as the cylindrical space enclosed between the two endcaps. Cladding A and B with their respective endcaps are shown in Figure 6.

2.3. Sample fabrication via capillary impregnation

The atomised matrix powder, fuel elements and selected cladding tubes were transferred into a high-purity argon atmosphere glovebox (Ar purity >99.998 %) for filling. Within the glovebox, cladding segments were first filled with fuel elements using vibratory insertion, before backfilling with the matrix powder until the internal volume was entirely

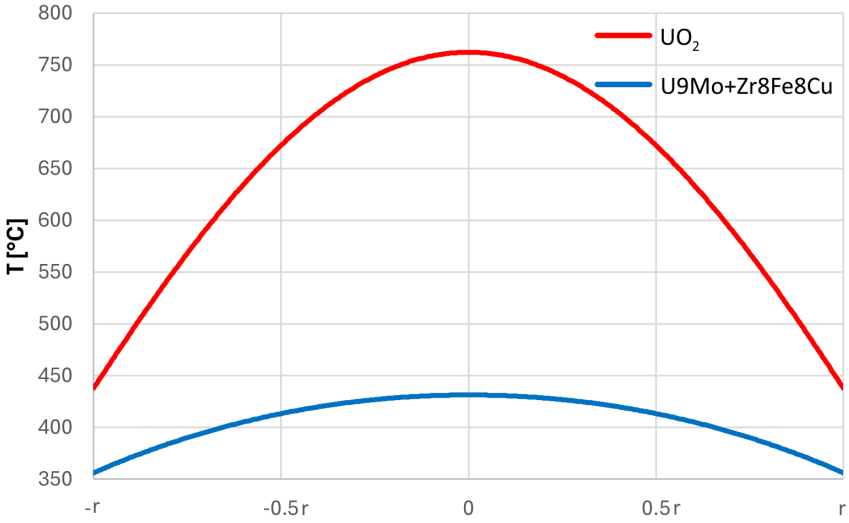

FIGURE 4. Calculated temperature profiles of UO_2 and U-9Mo.

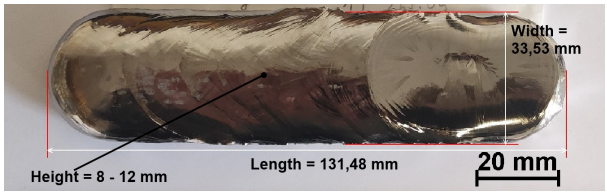

FIGURE 5. Geometry and dimensions of an arc-melted Zr-8Fe-8Cu ingot.

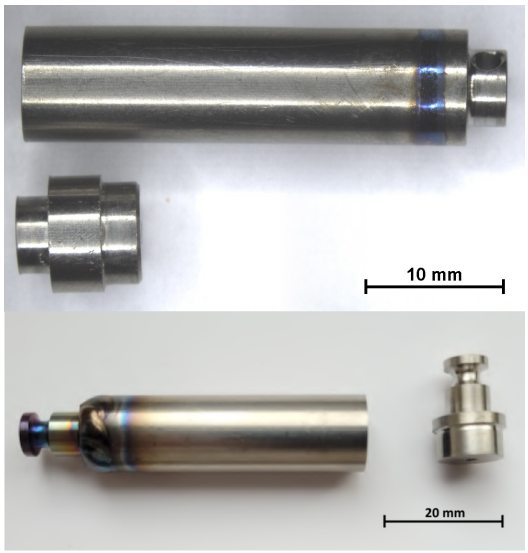

FIGURE 6. Cladding segments A (top) and B (bottom) before filling.

occupied. Supersonic vibration of samples during filling facilitated a uniform distribution of both fuel and matrix materials.

Once filled, the open end of each sample was closed off with an endcap and immediately upon removal from the inert atmosphere the cap was spot-welded in place to preserve internal integrity and prevent contamination. The completed samples were then subjected to a heat treatment process, known as capillary impregnation, in which they were heated to approximately 910 °C and held for 5 minutes to ensure uniform matrix infiltration by capillary action as is illustrated in Figure 7.

Four samples fabricated with Cladding A – HDF-U-1 to 3 and HDF-W-1, corresponding to the fuel types listed in Section 2.1 – as well as one additional sample combining Cladding B with depleted uranium elements for a LOCA (Loss of coolant accident) simulation (see Section 2.6), were processed for further analysis. The end caps were removed and each segment was subsequently sectioned into two or three radial samples (three sections weren't achieved with all 5 samples due to geometric constraints and proces related complications). The metallographic cross-sections were then prepared using standard mounting and polishing procedures.

2.4. METALLOGRAPHIC PREPARATION

Four samples fabricated with Cladding A – HDF-U-1 to 3 and HDF-W-1, corresponding to the fuel types listed in Section 2.1 – as well as one additional sample combining Cladding B with depleted uranium elements for LOCA simulation (see Section 2.6), were processed for further analysis. After heat treatment, the end caps were removed and each segment was subsequently sectioned into two radial samples using a xyz saw. The metallographic cross-sections were then prepared using standard mounting, grinding, and polishing procedures.

2.5. MICROSTRUCTURAL CHARACTERISATION

As-fabricated cross-sections were analyzed using a JEOL JSM-5510 scanning electron microscope in backscattered electron (BSE) mode to document microstructural features. Image segmentation with NIS-Elements was performed to quantify the relative area

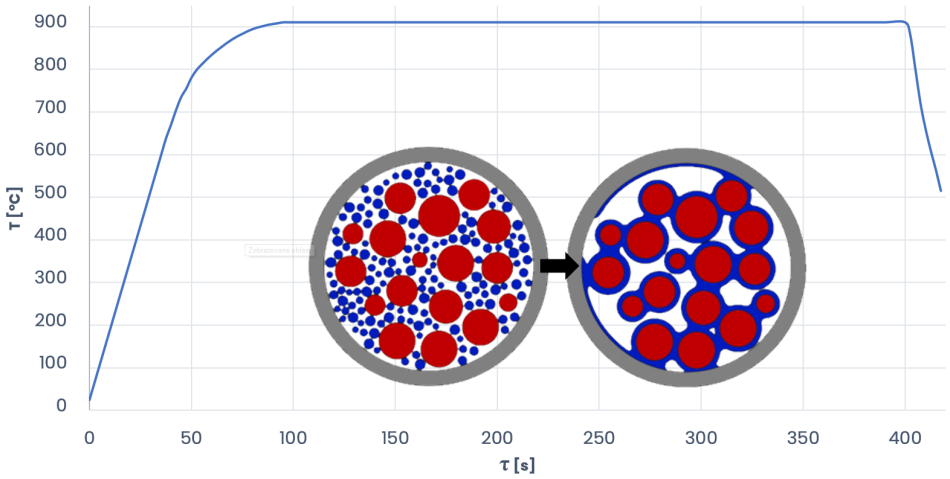

Figure 7. Capillary impregnation heat treatment.

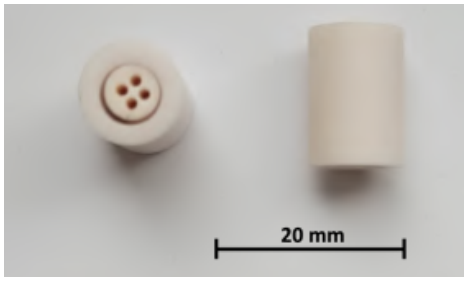

Figure 8. Allumina pellet prior to insertion between fuel-matrix mixture and endcap.

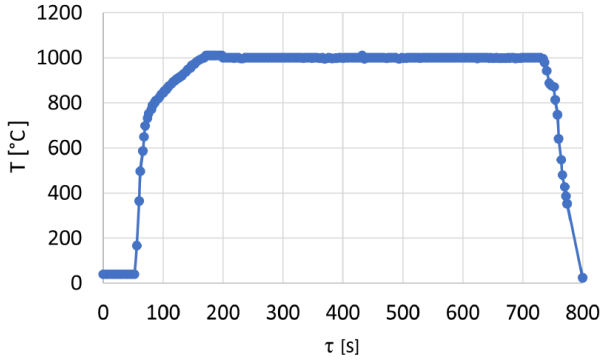

Figure 9. Temperature profile of LOCA experiment.

fractions of fuel, matrix, and porosity across all sections. Phase distribution and potential diffusion effects at fuel-matrix and matrix-cladding interfaces were investigated using energy-dispersive X-ray spectroscopy (EDS). This analysis provided insight into microstructural homogeneity, phase distribution, and metallurgical stability of the various fuel-matrix systems.

2.6. Simulated LOCA conditions

A unique sample was prepared and subjected to an experiment designed to simulate a large break loss-of-coolant accident (LB-LOCA). After partial filling with unalloyed uranium elements and matrix cutting chips, an alumina pellet with an outer diameter of 10.4 mm and a length of 15.1 mm shown in Figure 8 was used to buffer the fuel and matrix against overheating when sealing the second cap. The complete sealing of the sample was carried out by TIG welding the end cap to the sample at ambient pressure. The sample was subsequently impregnated at 905–910 °C for 2–5 minutes (shorter heating cycle to minimise creep deformation) and subjected to a thermal transient representative of LOCA conditions.

During LOCA, the pressure inside the reactor instantly drops and the cladding temperature rapidly grows up to (in case of high burnup even over) 1 000 °C before leveling off until the activation of backup cooling systems. For the experiment the sample is first heated to 1 000 °C and following a 10 minute hold it is water-quenched to simulate the activation of redundant cooling systems. The temperature profile measured with a type K thermocouple can be seen in Figure 9.

Post-LOCA analysis included stereomicroscopy using a Leica M205 C microscope to document macrostructural changes. Relocation of matrix material and qualitative observations of LOCA behaviour were recorded. EDS analysis was used to assess uranium diffusion and potential chemical erosion at the fuel-matrix and matrix-cladding interfaces.

2.7. Simulation of internal fuel temperature profile

To calculate the average temperature and temperature profile of the fuel for conventional UO_2 and the U-9Mo dispersion fuel (selected due to its good combination of uranium density and operational properties), a reference geometry of the fuel rod and fuel assembly of the VVER-1000 reactor was considered (ID = 7.72 mm, OD = 9.13 mm, and rod pitch 12.75 mm). The basic operating parameters were also adopted: average linear heat rate of the rod 16 kW m^{-1}, coolant pressure 15.7 MPa, and inlet coolant temperature 300 °C.

The same Zr1Nb alloy without an oxide layer was considered as the cladding material in both cases (the effect of the oxide layer is negligible due to its small thickness).

To obtain the boundary temperature of the fuel pellets (i.e., the outer pellet surface temperature to allow comparison for temperature profiles within the fuel matrix), the FRAPCON 3.4 fuel thermomechanical code was used. Typical VVER-1000 operational and fuel geometry parameters were used and the resulting average coolant temperature at mid-core height was calculated as 316.25 °C. The outer cladding temperature was found to be 330.13 °C, and the inner cladding temperature was 355.75 °C. For conventional UO_2 fuel with a fuel-cladding gap, a pellet diameter of 7.57 mm and a helium-filled gap with a fill pressure of 2 MPa were assumed. The surface temperature of the pellet is 436.29 °C. For the dispersion fuel based on U-Mo, the outer diameter of the "pellet" matched the inner diameter of the cladding (and thus the temperature was also identical). This approach is non-realistic but allows for a direct unbiased comparison thermal response of both fuel matrices at a given local power which is crucial for the fuel rod design and limits any effects of burnup/coolant/heat transfer variations that would complicate the comparison.

The calculation of the average volumetric fuel temperature was based on an analytical model of steady-state one-dimensional radial conduction in a cylinder with uniformly distributed internal heat sources, in a material whose thermal conductivity coefficient is linearly dependent on temperature which is valid assumption for metallic materials in the temperature range of interest. For accidental conditions, experimental evaluations of thermal conductivity are needed to improve accuracy but for nominal operation, this approach is valid.

$$\lambda(t) = \lambda_0 \left(1 + bt\right), \tag{3}$$

where:

b – constant describing the dependence of thermal conductivity on temperature [K^{-1}]

λ_0 – reference thermal conductivity [$W\,mK^{-1}$]

Analytical solution of Fourier's heat conduction differential equation with thermal conductivity presented in Equation 3 results in temperature profile takes the form:

$$t(r) = -\frac{1}{b} + \frac{1}{b}\sqrt{1 + 2b\left[\frac{q_v}{4\lambda_0}\left(R^2 - r^2\right) + t_p\left(1 + \frac{b}{2}t_p\right)\right]}, \tag{4}$$

where:

q_v – volumetric heat generation rate [$W\,m^{-3}$]

R – fuel pellet radius [m]

t_p – fuel surface temperature, see above [°C]

Using the outer surface fuel pellet temperature calculated using FRAPCON as a boundary condition, one can determine the temperature distribution in the matrix and compare it directly to the reference case.

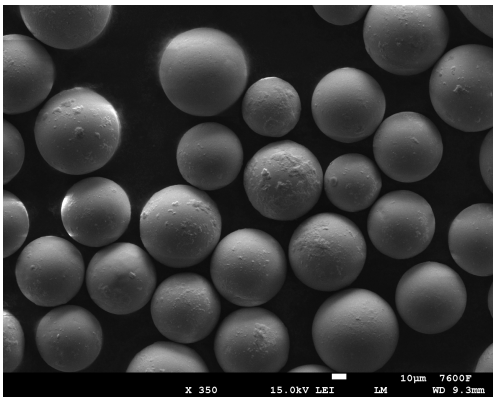

FIGURE 10. Atomised matrix particles.

For the calculation of fresh fuel at a density of 95 % TD, the thermal conductivity model for UO_2 recommended in [5] was chosen as a reference.

The following volume fractions of the individual components were considered for the U-Mo fuel calculation:

U-9Mo: 52.7 %

Zr8Fe8Cu matrix: 29.77 %

Voids/pores: 17.52 %

For some of these, no precise equations for determining thermal conductivity are available in the literature, so values were extracted from graphical data in [6].

3. RESULTS

3.1. COMPARISON OF CALCULATED FUEL TEMPERATURE PROFILES

The results of the numerical calculations for both fuel types are plotted in Figure 4. The centerline (peak) temperature of the dispersion fuel (431.37 °C) is over 330 °C lower than that of UO2-based pellets (762.63 °C). It should be noted that this is a best-case comparison for the oxide fuel as with increasing burnup its thermal conductivity drops significantly faster and the peak operational temperature can reach well over 1 000 °C.

3.2. CHARACTERISATION OF MATRIX POWDER

An SEM (scanning electron microscope) secondary electron image of the atomised matrix can be seen in Figure 10. The powder displayed low exccentricity as well as minimal satelite presence and a relatively good particle size distribution. The surface of the powder appears to present some signs of oxidation, albeit minimal due to careful handling.

Chemical composition of 3 powder particles was measured via EDS (Energy-Dispersive Spectroscopy) with the results included in Table 2. While 2 of the results show a lower than expected Fe and Cu content, prior matrix analysis showed formation of multiple phases (= eutectic structure) during solidification.

	Zr [wt. %]	Fe [wt. %]	Cu [wt. %]
Spot 1	91.81	5.2	2.99
Spot 2	83.22	7.8	8.99
Spot 3	92.12	5.62	2.26

Table 2. EDS measurements of powder particles.

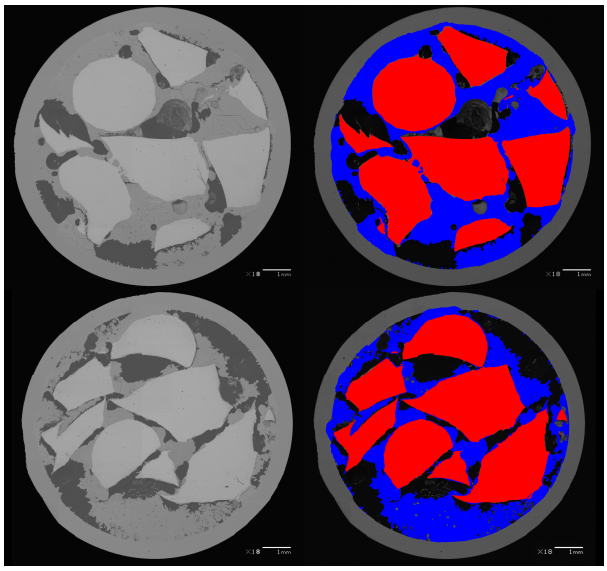

Figure 11. SEM images before (left) and after (right) segmentation of HDF-U-1A (top) and HDF-U-1B (bottom).

	Fuel [%]	Matrix [%]	Porosity [%]
HDF-U-1A	47.1	32.9	20
HDF-U-1B	45.5	29.6	24.9
Average	46.3	31.3	22.5

Table 3. Fuel, matrix and porosity area ratios of sample HDF-U-1.

3.3. HDF sample analysis

3.3.1. Uranium (HDF-U-1)

Figure 11 presents SEM backscattered electron (BSE) images of sample HDF-U-1 along with corresponding segmented images, clearly differentiating fuel particles (red), metallic matrix (blue), and porosity (black).

The fuel particles exhibit irregular shapes with sharp boundaries, while the metallic matrix shows relatively uniform distribution throughout the sample cross-section. Porosity appears dispersed within the matrix without significant preference for fuel particles or inner cladding wall. The quantitative area fractions obtained from image analysis are summarized in Table 3.

Assuming uranium density of 19.1 gU cm^{-3} (density of pure uranium metal), the achieved fissile material density of the manufactured sample falls between 8.7 and 9 gU cm^{-3}, which is comparable to the fuel density of current systems.

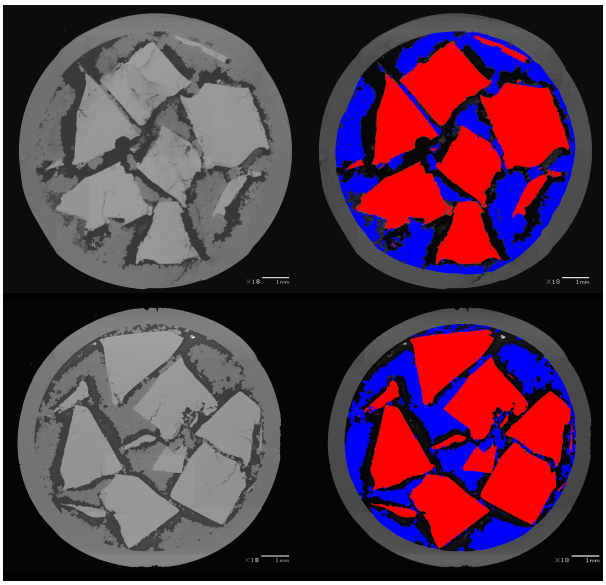

Figure 12. SEM images before (left) and after (right) segmentation of HDF-U-2A (top) and HDF-U-2B (bottom).

	Fuel [%]	Matrix [%]	Porosity [%]
HDF-U-2A	46.5	27	26.5
HDF-U-2B	49.1	25.9	25
Average	47.8	26.5	25.8

Table 4. Fuel, matrix and porosity area ratios of sample HDF-U-2.

3.3.2. U-9Mo (HDF-U-2)

Figure 12 shows SEM images and corresponding segmented representations for sample HDF-U-2, prepared from a U-Mo alloy.

The U-Mo fuel particles display more regular shapes with less sample-to-sample variation. While the matrix material is consistently distributed around fuel particles, porosity is notably more concentrated at particle-matrix interfaces compared to sample HDF-U-1, suggesting possible interface interactions or excess oxidation during capillary impregnation. The measured data is summarized in Table 4.

Given the uranium density of U-9Mo (15.5 gU cm^{-3}), the resulting fissile material density in the fabricated fuel sample ranges from 7.2 to 7.6 gU cm^{-3}.

3.3.3. U-4Si (HDF-U-3)

Figure 13 shows SEM images and segmented views for sample HDF-U-3. The irregular fuel particles show significantly more cracking compared to previous samples, indicative of increased brittleness inherent to U-Si alloys and the method used for their preparation. Additionally, substantial variability in fuel-to-matrix ratios between different sections was observed, likely caused by the wide particle size distribution and subsequent segregation of smaller particles towards the bottom as a result of vibration loading during fabri-

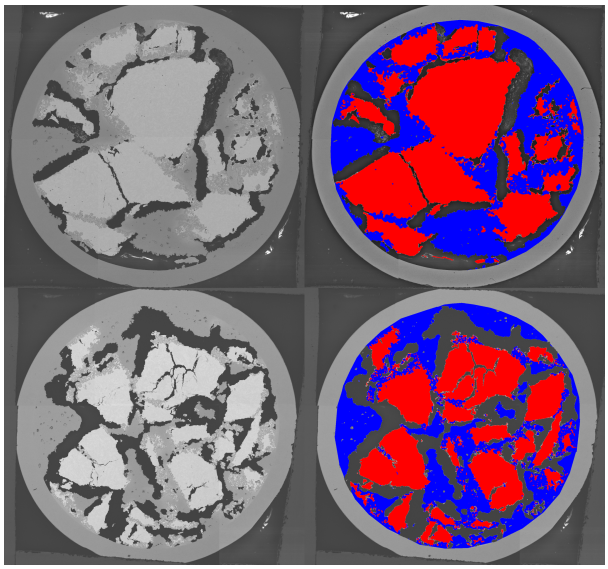

FIGURE 13. SEM images before (left) and after (right) segmentation of HDF-U-3A (top) and HDF-U-3B (bottom).

	Fuel [%]	**Matrix** [%]	**Porosity** [%]
HDF-U-3A	47.5	32.5	20
HDF-U-3B	37.5	31.3	31.2
Average	42.5	31.9	25.6

TABLE 5. Fuel, matrix and porosity area ratios of sample HDF-U-3.

cation. The metallic matrix maintains a generally homogeneous distribution despite significant differences in observed fuel and porosity ratios. Segmentation results can be found in Table 5.

By applying the law of mixtures, the uranium density of U-4Si can be approximated as $14.2\,\mathrm{gU\,cm^{-3}}$. Consequently, the fissile density of the manufactured sample ranges from 5.3 to $6.75\,\mathrm{gU\,cm^{-3}}$.

3.3.4. Tungsten (HDF-W-1)

SEM BSE images and their corresponding segmented counterparts for sample HDF-W-1 are shown in Figure 14. The tungsten elements are uniformly distributed with a significant improvement in packing density over the remaining samples, resulting in a significantly higher fuel content compared to previous samples. Both the metallic matrix and porosity are also evenly distributed across the sample, highlighting the effectiveness of spherical particle geometry in achieving a highly homogeneous microstructure. Quantified area fractions are listed in Table 6.

3.3.5. Summary

Table 7 summarizes the average fuel, matrix, and porosity fractions derived from the previous analysis, along with the equivalent uranium densities for each sample (except for sample HDF-W-1, whose equivalent density is listed in Table 8).

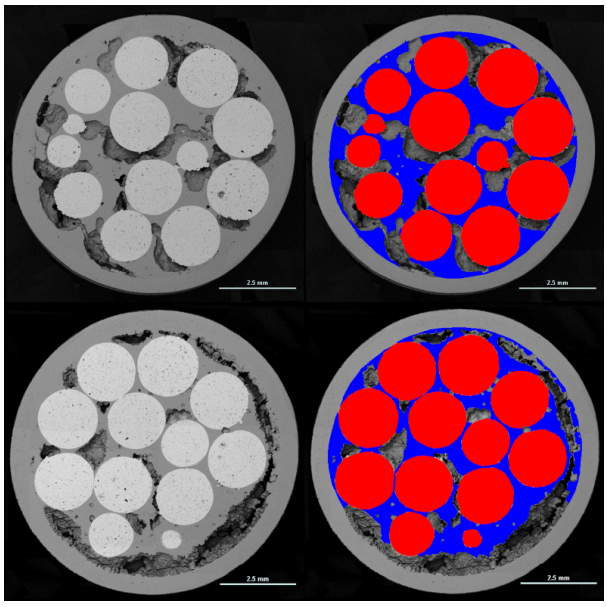

FIGURE 14. SEM images before (left) and after (right) segmentation of HDF-W-1A (top) and HDF-W-1B (bottom).

	Fuel [%]	**Matrix** [%]	**Porosity** [%]
HDF-W-1A	56.9	23.1	20
HDF-W-1B	57.6	22.1	20.3
Average	57.3	22.6	20.2

TABLE 6. Fuel, matrix and porosity area ratios of sample HDF-W-1.

	Fuel [%]	**Matrix** [%]	**Pores** [%]	**U** [$\mathbf{gU\,cm^{-3}}$]
HDF-U-1	46.3	31.3	22.5	8.9
HDF-U-2	47.8	26.5	25.8	7.4
HDF-U-3	42.5	31.9	25.6	6
HDF-W-1	57.3	22.6	20.2	Tab 8

TABLE 7. Summary of averaged fuel, matrix and pore area fractions.

Alloy	**Equivalent uranium density** [$\mathbf{gU\,cm^{-3}}$]
Uranium	10.9–11
U-9Mo	8.8–8.9
U-4Si	8.1–8.2

TABLE 8. Extrapolated uranium densities given spherical fuel geometry.

Table 8 lists the equivalent uranium density of the three selected uranium alloys assuming sample HDF-W-1 geometry.

3.4. Post-LOCA evaluation

Following the simulated LB-LOCA experiment, the test sample was examined to assess structural and chemical changes induced by matrix overheating and thermal shock. Stereomicroscopy revealed visible macrostructural changes, including significant relo-

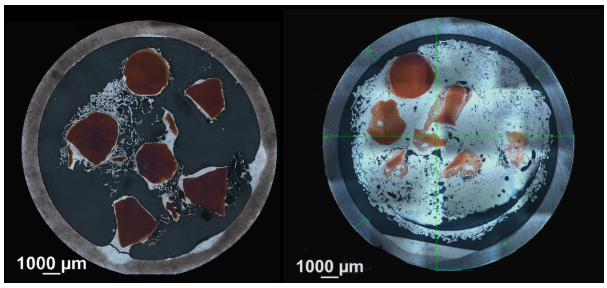

Figure 15. Radial sections of the top (left) and bottom (right) of the sample after simulated LOCA.

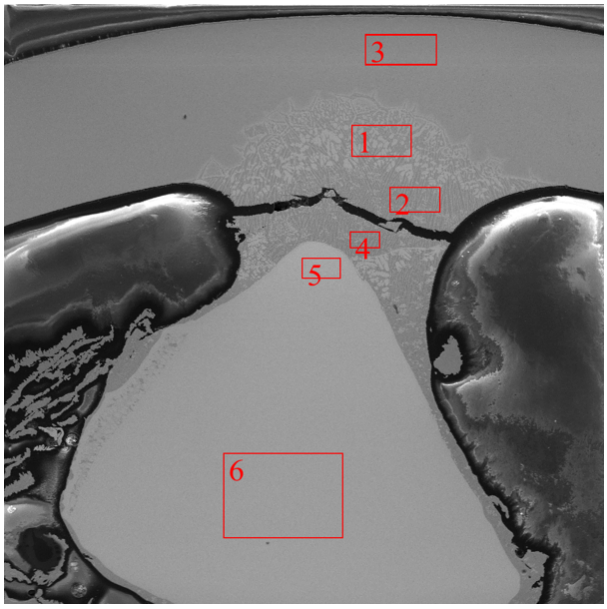

	U [wt. %]	Zr [%]	Fe [%]	Cu [%]
1	29.98	59.17	1.89	8.96
2	23.78	60.78	3.13	12.31
3	0.35	98.83	0.32	0.4
4	23.31	61.29	2.8	12.6
5	96.72	2.59	0.56	0.13
6	97.47	1.91	0.29	0.34

Figure 16. Matrix-cladding interaction.

cation of the matrix under gravity due to reduced viscosity, as shown in Figure 15. It should be noted that, since the sample incorporated matrix cutting chips instead of powder, its matrix content was suboptimal and matrix relocation was therefore exaggerated.

While no rupture of the cladding was observed, SEM examination revealed substantial localized deleterious interactions at the matrix-cladding interface. Figure 16 shows the most severe of these, where approximately half of the cladding wall thickness was compromised due to matrix dissolution. Concurrently, significant diffusion of uranium into the matrix. As a result some uranium diffusion into the cladding was also seen .

It should be noted that the simulated LOCA conditions are based on current reactors using sintered UO_2 fuel, which – as shown in Section 3.1 – operate at higher temperatures and possess a higher specific heat capacity. As a result, the thermal loading experienced by the tested high-density fuels under comparable accident conditions would likely be less severe.

4. Conclusions

This work presents a comparative evaluation of several metal-based high-density fuel (HDF) concepts, focusing on their microstructural characteristics and behavior under simulated accident conditions.

High-density fuel samples were successfully fabricated using three different uranium alloys and a tungsten-based pseudoalloy. Metallographic and chemical analyses revealed clear differences in fuel distribution, porosity, and matrix stability across the various compositions, with spherical fuel geometries producing the most homogeneous microstructures. The highest recorded area fraction of fuel simulator particles, 56.9–57.6 %, was observed in sample HDF-W-1, which would correspond to a uranium density of approximately 8.8–8.9 gU cm^{-3} if fabricated with U-9Mo or 8.1–8.2 gU cm^{-3} if made with U-4Si. Even higher densities could be achieved using smaller-diameter spheres, with the theoretical packing limit approaching 74 %.

The LOCA experiment demonstrated the potential for deleterious matrix–cladding interactions at elevated temperatures, underscoring the importance of metallurgical compatibility in future fuel designs. Significant diffusion of uranium into the Zr-based matrix was observed during the LOCA scenario, and to a lesser extent during capillary impregnation. However, it is important to consider that the lower operating temperatures and heat capacity of advanced HDF systems may alter the severity and dynamics of accident scenarios in difficult-to-predict ways.

Acknowledgements

This contribution was supported by the Technology Agency of the Czech Republic under the research project NCK TN02000012 and is based on results achieved within the THÉTA project TK03020034. Thermal analysis was contributed by Martin Ševeček from the Faculty of Nuclear Sciences and Physical Engineering (Czech Technical University in Prague) and the LOCA sample was prepared and analysed by Martin Přibyl. My appreciation goes to R. Findell for his preparation exercise.

References

[1] S. El Jamal, M. Johnsson, M. Jonsson. On the stability of uranium carbide in aqueous solution – Effects of HCO_3^- and H_2O_2. *ACS Omega* **6**(37):24289–24295, 2021. https://doi.org/10.1021/acsomega.1c04581

[2] C. Ekberg, D. Ribeiro Costa, M. Hedberg, M. Jolkkonen. Nitride fuel for Gen IV nuclear power systems. *Journal of Radioanalytical and Nuclear Chemistry* **318**:1713–1725, 2018. https://doi.org/10.1007/s10967-018-6316-0

[3] A. Savchenko, I. Konovalov, A. Vatulin, et al. Dispersion type zirconium matrix fuels fabricated by capillary impregnation method. *Journal of Nuclear Materials* **362**(2):356–363, 2007. E-MRS 2006: Symposium N. https://doi.org/10.1016/j.jnucmat.2007.01.211

[4] A. M. Savchenko, Y. V. Konovalov, A. V. Laushkin, G. V. Kulakov. Zirconium alloys with low melting points. *Inorganic Materials: Applied Research* **10**:1471–1476, 2019. https://doi.org/10.1134/S2075113319060212

[5] International Atomic Energy Agency. *Thermophysical properties database of materials for light water reactors and heavy water reactors*. Vienna, 2006. AEA-TECDOC-1496, ISBN 92–0–104706–1.

[6] Suwardi. Advanced fabrication technique and thermal performance prediction of U-Mo/Zr-alloy dispersion fuel pin for high burnup PWR. *AIP Conference Proceedings* **1244**(1):145–155, 2010. https://doi.org/10.1063/1.3462752